applied sciences

MDPI

Article

Microstructure and Fracture Behaviors of Oscillating Laser Welded 5A06 Aluminum Alloy Lock Butt Joint

Yang Lu [1], Jian Lai [2], Junping Pang [2], Xin Li [1], Chen Zhang [3,*] and Ming Gao [1,*]

1 Wuhan National Laboratory for Optoelectronics, Huazhong University of Science and Technology, Wuhan 430074, China
2 Hangzhou Dongcheng Electronic, Hangzhou 310009, China
3 The Institute of Technological Sciences, Wuhan University, Wuhan 430072, China
* Correspondence: c.zhang@whu.edu.cn (C.Z.); mgao@mail.hust.edu.cn (M.G.)

Abstract: Oscillating laser welding is potential to improve the quality of aluminum alloy joints, but has been seldom addressed on lock butt joint. In this paper, the effects of beam oscillation frequencies (f) on the properties of laser-welded 5A06 aluminum alloy lock butt joints were investigated, especially those at the lock step. In the microstructure, the columnar grain zone (CGZ) near the fusion line narrowed, the porosity was reduced, and the angle between lock step and fusion line increased with the increase of f. Correspondingly, the fracture changed from equiaxed grain zone to heat affected zone (HAZ), and the fracture angle between lock step and crack propagation line from 90° to 45°. The maximum ultimate tensile strength and elongation of oscillating weld reached 308 MPa and 18.2%, respectively, 36.3% and 203.3% higher than non-oscillating weld. The fracture behaviors indicated that the crack always initiated at the lock step, and then preferably propagated to the pores, followed closely by the weaker CGZ, and then the stronger HAZ when CGZ was narrowed enough. Notably, when the pore size was small (<0.39 mm) and located below the lock step, the pore was not on the crack propagation path. The crack tended to propagate towards the weaker CGZ. Finally, the fracture mechanism was discussed. The results clarify the fracture mechanism of oscillating laser-welded lock butt joints and contribute to the development of oscillating laser welding.

Keywords: laser welding; beam oscillation; aluminum alloy; lock bottom weld; fracture

Citation: Lu, Y.; Lai, J.; Pang, J.; Li, X.; Zhang, C.; Gao, M. Microstructure and Fracture Behaviors of Oscillating Laser Welded 5A06 Aluminum Alloy Lock Butt Joint. *Appl. Sci.* **2023**, *13*, 3381. https://doi.org/10.3390/app13063381

Academic Editors: Ricardo Branco, Joel De Jesus and Diogo Neto

Received: 3 January 2023
Revised: 1 March 2023
Accepted: 5 March 2023
Published: 7 March 2023

1. Introduction

The 5A06 aluminum alloy, as one type of high-strength Al-Mg alloy, has been widely used in automobiles, shipbuilding, aerospace engineering, and high-speed trains, due to its high strength-to-weight ratio [1–3]. Laser welding has the advantages of lower heat input, high energy intensity, narrow heat-affected zone (HAZ) and high welding speed, which is very suitable for joining dissimilar alloys and large-scale manufacturing areas [4–7]. However, the intensive susceptibility to pores restricts the application of Al alloy laser welding [8–10], especially for load-bearing structures with lock bottom welds, which are the main joint form for ensuring the consistency of weld morphology and quality in manufacturing of pipelines and missile structures [11,12]. In the lock bottom structure, the thick side of the base metal is prepared with the process step as the back support for the thin side of the base metal. For this non-penetration welding structure, the keyhole induces a closed vortex at the root, resulting in bubbles in this area being unable to escape by the root melt flow as effectively as in welds with full penetration, and it is therefore easier to form pore defects [13]. Tan et al. studied 5A06 Al alloy lock bottom welds using laser welding with fixed laser power. The results showed that the weld had uneven surface forming and internal pore defects [14]. In addition, because the Mg element is the most important and easiest to burn in 5A06 aluminum alloy, laser welding may lead to the deficiency or segregation of Mg element [15]. Therefore, how to solve these issues has been a research hotspot in the field of aluminum alloy laser welding.

In recent years, some scholars have proved that oscillating laser welding is helpful to solve the pore problem of aluminum alloys with non-penetration welds. Liu et al. found that the fluctuation of the melt flow at f = 100 Hz is the smallest in oscillating laser welding of 7075 aluminum alloy, thereby improving the keyhole stability and reducing the porosity [16]. In the study of sinusoidal oscillating laser welded 6061/5182 Al alloy sheets, Chen et al. obtained porosity-free welds in the non-penetration state [17]. Fetzer et al. used online X-ray imaging to detect the bubble movement in oscillating laser welding of AlMgSi alloy. They observed that bubbles in the molten pool were captured by the oscillating keyhole and disappeared at f = 100 Hz [18]. The previous research of our team revealed that the keyhole scanning speed threshold, which can effectively suppress the pores of non-penetration 5A06 Al alloy welds, decreased with the increasing oscillation radius [19].

Moreover, oscillating laser welding has positive impacts on the microstructure and properties of Al alloy welds. For the butt welding, Bi et al. found that beam oscillation can realize the comprehensive control of melt flow and temperature field in the laser welding of Al-Li alloys, thus reducing element segregation [20]. Hu et al. found that oscillating laser welding of AA2060 and AA6061 with a circular pattern can reduce the width of the equiaxed grain zone at the AA2060 side and increase the tensile strength, because the convection generated by the laser beam stirring effect can displace the heterogeneous nucleation particles from the edge to the weld center [21]. Wang et al. revealed that the strong stirring effect of the laser beam on the molten pool can increase the equiaxed grains content inside the 6061 Al alloy weld, and significantly improve the tensile elongation [22]. For the lock bottom welds, Wang et al. found that the infinity oscillating mode was the most conducive to reducing the porosity of 5A06 Al alloy and increasing tensile strength. However, the effects of porosity and microstructure evolution on fracture behavior with different oscillating parameters were not involved in this study [23]. Li et al. proved that the suppression effect of circular beam oscillation on pores was the main reason for the improvement of 5083 Al welding mechanical properties. However, the strengthening mechanism of this study was established based on the butt weld instead of lock bottom structure, and the microstructure variation near lock step and fracture behavior of the lock bottom weld were ignored, which played an important role in mechanical properties [24].

The above research showed that oscillating laser welding can inhibit the pores of unpenetrated Al welds, improve their microstructure, and then increase their properties. However, few studies have been conducted on oscillating laser welding of Al alloys in lock bottom configuration. Due to the special structure of the lock step, weld characteristics similar to the kissing bonding in friction stir welding will be formed in the lap part of the lock bottom weld. Deng et al. studied the fracture behavior of NiTi/Ti6Al4V joints and found that the kissing bonding was the main factor for deteriorating the mechanical properties of joints [25]. This work, therefore, studied the effects of laser beam oscillation on the lock bottom weld of 5A06 Al alloy, and focused on the microstructure characterizations and fracture behaviors near the lock step.

2. Experimental

The base metals (BM) were 6 mm and 3 mm thick 5A06 Al alloy, and their chemical composition is presented in Table 1. Before welding, the sheets were polished to remove the oxide film and impurities on the surface and then cleaned with acetone. The experimental setup is shown in Figure 1: the laser beam was transmitted from an IPG YLR-6000 fiber laser with the maximum output power of 6 kW, collimated by a 200 mm focal length lens unit, reflected by a copper mirror, deflected by the X/Y galvanometer scanner units, and finally focused by an f-theta focus lens with a focal length of 250 mm. The radius of focused laser beam spot was about 0.167 mm. In this study, the circular oscillating pattern was selected according to reported research [26]. During welding, the weld surface was protected by 99.99% Argon shielding gas at a flow rate of 25 L/min. The welding speed (v) was 2 m/min. Other processing parameters were listed in Table 2.

Table 1. Chemical composition (wt.%) of 5A06 Al alloy [27].

Element	Si	Fe	Cu	Mn	Mg	Zn	Ti	Al
Content	0.4	0.4	0.1	0.5	6.8	0.2	0.02	Bal

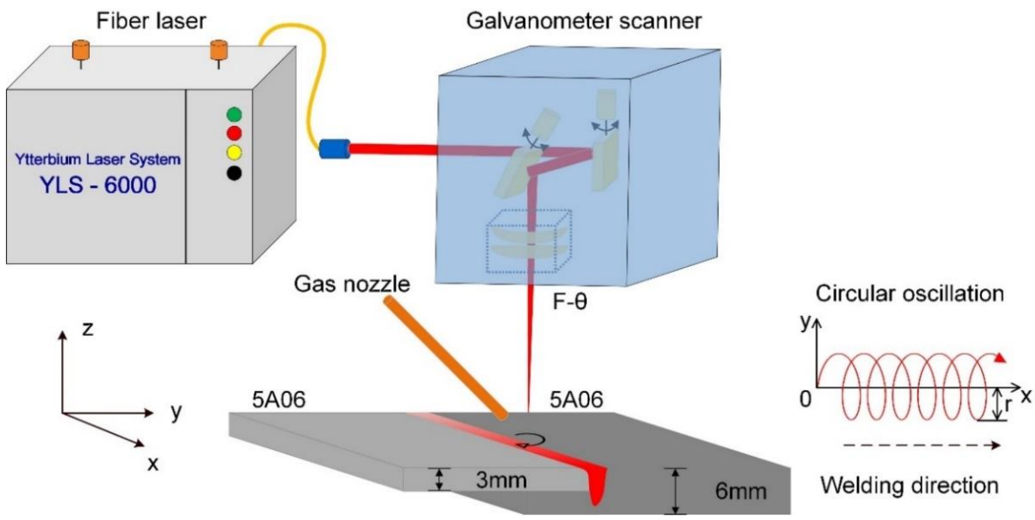

Figure 1. Oscillating laser beam welding system of 5A06 alloy lock bottom weld.

Table 2. The processing parameters, where P denotes laser power, v denotes welding speed and r and f denote oscillation radius and frequency, respectively.

Welding Parameters	#1	#2	#3	#4	#5	#6	#7	#8	#9	#10	#11
P (kW)	3.0	3.5	3.5	3.5	3.5	3.5	3.5	3.5	3.5	3.5	3.5
v (m min^{-1})	2.0	2.0	2.0	2.0	2.0	2.0	2.0	2.0	2.0	2.0	2.0
r (mm)	-	0.6	0.6	0.6	0.6	0.6	0.6	0.6	0.4	0.8	1.0
f (Hz)	-	50	100	150	200	250	300	350	200	200	200

After welding, the cross-section specimens for microstructure observation were sectioned in the center area of the weld. The microstructure was observed by optical microscope (OM) and electron backscatter diffraction (EBSD), and the observation positions are near the lock step. The metallurgical specimens for OM were grinded using emery papers with grit sizes varying from 400 to 2000, then rinsed with water and subsequently polished with diamond paste suspension. After that, they were etched with a solution of 1 mL HF, 1.5 mL HCl, 2.5 mL HNO_3 and 95 mL H_2O at room temperature for 20 s. The EBSD specimens were grinded and then electropolished with an electrolyte of 10 mL perchloric acid and 90 mL ethanol. The dimensions of tensile testing specimens are shown in Figure 2. A heel block was added on the thin side of the plate to ensuring that the clamping thickness of specimen was consistent. The tensile tests were carried out at room temperature, and the results were the average of three specimens. The fracture morphologies were investigated by scanning electron microscopy (SEM).

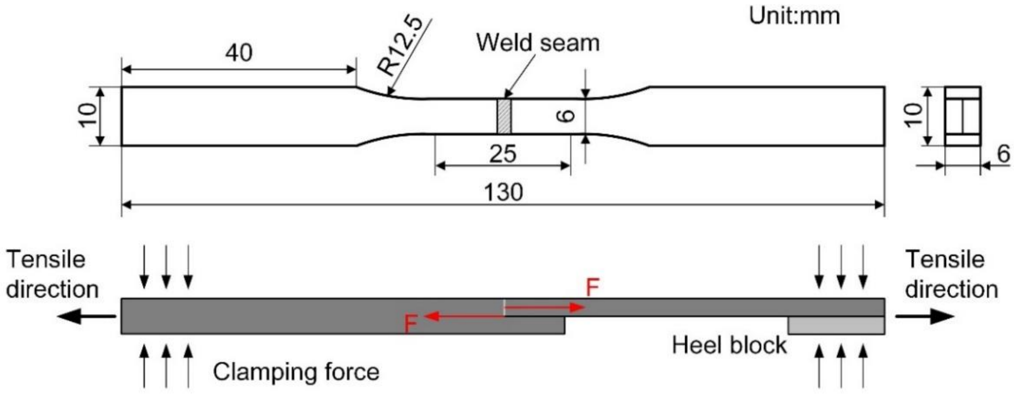

Figure 2. Schematic diagram of tensile specimens.

3. Results and Discussion

3.1. Weld Morphology

Figure 3 showed the surface, cross-section morphologies and X-ray nondestructive test results. Compared with the non-oscillating weld, when f = 50 Hz, which increased to a small extent, the effect of the laser beam oscillation was not obvious. As a result, there was little change in the weld morphology, which had undercut and uneven fish scale defects. As f increased, the weld surface quality continuously improved. When f increased to 350 Hz, there were no undercut or concave defects, and the fish scales were uniform. The angle between the lock step and fusion line increased with f, and the porosity showed the opposite trend. In detail, with r fixed as 0.6 mm, the state of pores changed from close-packed chain-shaped to dispersed distribution until they were fully eliminated when f was in the range of less than 200 Hz, 200~350 Hz and more than 350 Hz, respectively. Notably, when f = 50 Hz, the porosity increased compared with the non-oscillating weld. The pores of non-oscillation and low oscillating frequency (f = 50 Hz) welds are located at the center line of welds, but the former are located above the lock step, and the latter are close to the bottom of molten pool (below the lock step), which is related to the cause of pores formation. The pores in non-oscillation welds are due to the turbulent flow formed by the confluence of the upper and lower vortexes [28]. The depth of the molten pool where the confluence located is similar to the height of the lock step. When f = 50 Hz, the keyhole stability is poor, resulting in the collapse of the keyhole root and pore formation. When f continues to increase, the keyhole stability is improved, and the pores can be captured. Therefore, the number and size of pores are reduced, and the position is not fixed. The threshold of f for pore suppression was 350 Hz, which was consistent with the results of bead-on-plate welding revealed in Ref. [19].

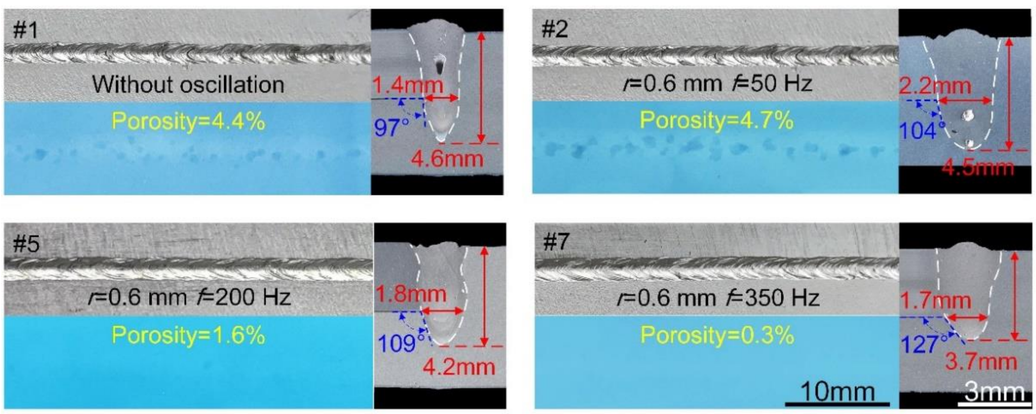

Figure 3. Weld morphology, P = 3.0/3.5 kW, v = 2 m/min.

3.2. Microstructure

Figure 4 shows the microstructure near the lock step. All welds were composed of columnar grain zone (CGZ), equiaxed grain zone (EQZ) and heat-affected zone (HAZ). By measuring the width of different regions, it can be found that the width of the CGZ for the weld without beam oscillation were 200 µm. But as shown in Figure 4c–e, the width of the CGZ gradually decreased with the increasing *f*. When *f* increased to 350 Hz, the width of the CGZ decreased to 54 µm, which was only 27% of the width of the CGZ without beam oscillation. In order to further analyze the grain size and morphology of the CGZ and EQZ, EBSD was performed, and the results are shown in Figure 5. For the non-oscillating weld, the average grain sizes of the CGZ and EQZ are 66.4 µm and 64.2 µm, respectively. When *f* increased to 350 Hz, the average grain sizes of CGZ and EQZ are 48.6 µm and 42.8 µm, which are 26.8% and 33.3% smaller than those of the non-oscillating weld.

The alloying elements in aluminum alloys have a boiling point lower than the molten pool temperature. During the laser welding process, these elements are lost due to evaporation, resulting in insufficient element content in the weld and reducing the performance of the weld. The Mg element is the most important, but also the easiest to burn, alloying element in 5A06 aluminum alloy. To study the distribution characteristics of alloying element Mg, the XRF test is carried out in the transverse and longitudinal directions of the weld, and the degree of segregation is evaluated by the standard deviation. The test position and results are shown in Figure 4 and Table 3, respectively. The results show that the average content of Mg element in the circular oscillating weld is 6.05% in the transverse direction and 6.12% in the longitudinal direction, accounting for 98.2% and 99.4% of the Mg element content (6.16%) in the BM respectively. In contrast, the content of Mg element in the transverse and longitudinal directions in the non-oscillating weld is 5.87% and 5.91% respectively, accounting for 95.3% and 95.9% of the Mg element content in the BM. In addition, the standard deviation of Mg element content in circular oscillating welds is smaller than that in non-oscillating welds. Therefore, circular oscillating laser welding greatly alleviates Mg element burning loss and makes the distribution of Mg element more uniform.

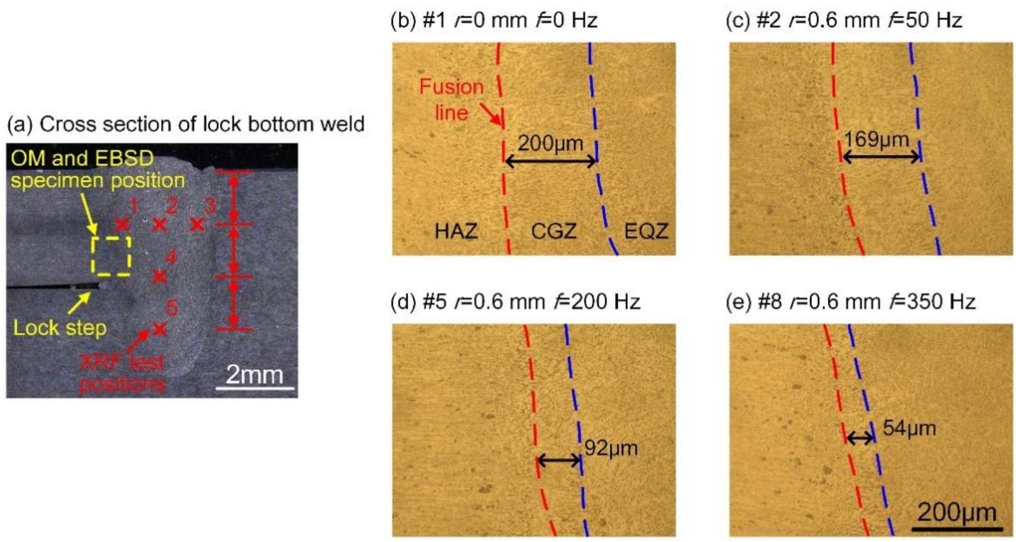

Figure 4. Microstructure near lock step, (**a**) cross section of lock bottom weld; (**b**) r = 0 mm, f = 0 Hz; (**c**) r = 0.6 mm, f = 50 Hz; (**d**) r = 0.6 mm, f = 200 Hz; (**e**) r = 0.6 mm, f = 350 Hz.

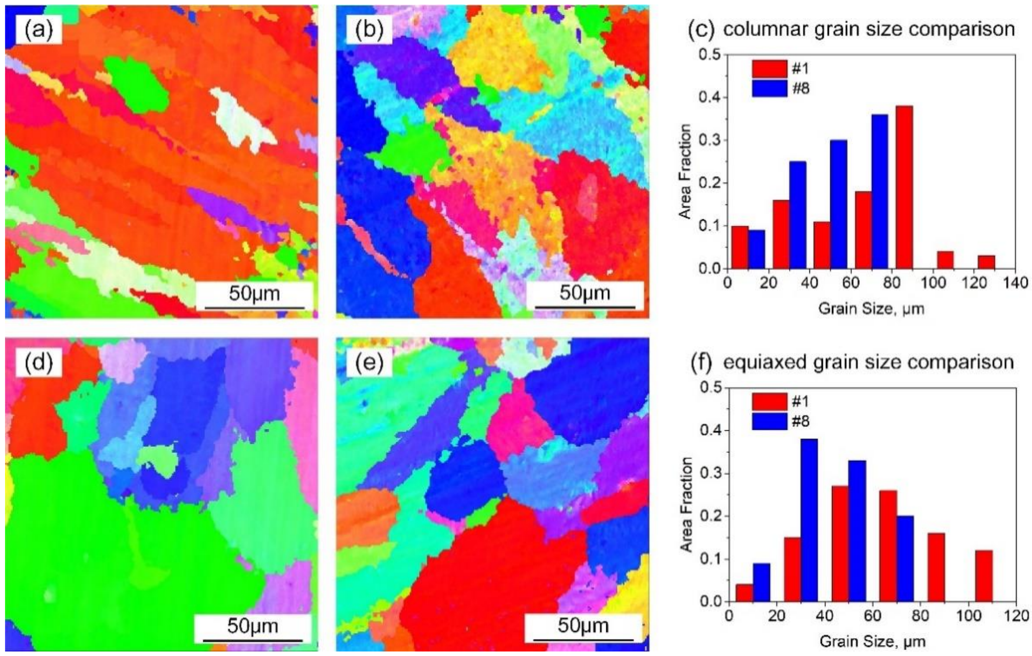

Figure 5. EBSD results of #1 and #8 welded joints, (**a**) IPF cross sections of CGZ in #1 weld; (**b**) IPF cross sections of CGZ in #8 weld; (**c**) statistical comparison of grain size distribution in CGZ of #1 and #8 welds; (**d**) IPF cross sections of EQZ in #1 weld; (**e**) IPF cross sections of EQZ in #8 weld; (**f**) statistical comparison of grain size distribution in EQZ of #1 and #8 welds.

Table 3. The test results of XRF in the weld.

Samples	Position	Mg	Stdev	
			Transverse	Longitudinal
BM-5A06	-	6.16	-	-
without oscillation	1	6.11	0.17	0.15
	2	5.8		
	3	5.71		
	4	5.8		
	5	6.13		
r = 0.6 mm f = 350 Hz	1	6.22	0.13	0.12
	2	6.02		
	3	5.91		
	4	6.06		
	5	6.29		

Figure 6 shows the effect of beam oscillation on the melt flow. For the weld without oscillation, as shown in Figure 6a, the laser energy was concentrated in the center and the temperature gradient of the molten pool was large, resulting in columnar grains on both sides of the weld. The melt flow was mainly affected by the Marangoni effect, whose speed was slow and the scouring effect on both sides of the weld was not obvious. Thus, the width and grain size of CGZ was large. The lock step was located at the waist of weld. The melt flow moved downward smoothly and the fusion line was straight, thus the angle between the fusion line and lock step was small. As shown in Figure 6b, the range of laser beam oscillation increased significantly with f, making the energy distribution more uniform and reducing the temperature gradient of molten pool greatly. This is also the reason why the burning loss of Mg element is alleviated. The strong stirring effect promoted the remelting and fragmentation of the CGZ, weakened and inhibited the growth of columnar grains, and thereby decreased the width and grain size of CGZ. It has been reported that a decrease of grain size leads to an increase of grain boundaries, which is beneficial to the diffusion of Mg elements [29]. At the same time, the beam stirring behavior can promote melt flow, resulting in uniform distribution of Mg elements in the weld. Moreover, the lock step was close to the bottom of weld, and the fusion line was just in the transition stage between the bottom and waist of the weld. The large bending degree of the fusion line enlarged the angle between lock step and fusion line.

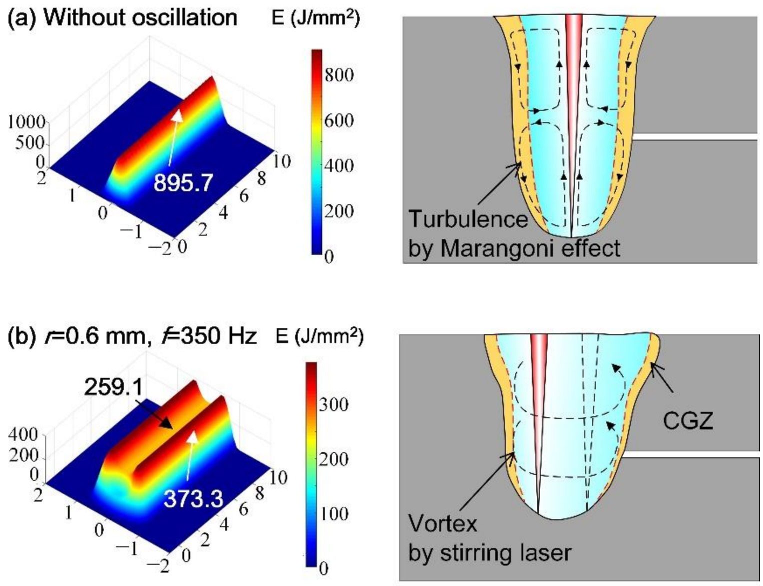

Figure 6. Schematic of the influence of beam oscillation on melt flow, (**a**) without oscillation, (**b**) r = 0.6 mm, f = 350 Hz.

3.3. Tensile Properties

As shown in Figure 7, for the weld without beam oscillation, the ultimate tensile strength (UTS) and elongation (EL) were 226 MPa and 6%, respectively. For the welds with beam oscillation, both UTS and EL increased with the f, and the best mechanical properties were achieved at f as 350 Hz, which were 308 MPa and 18.2%, respectively, reaching 96.3% and 86.6% of BM, respectively. Compared with the weld without beam oscillation, UTS and EL were increased by 36.3% and 203.3%, respectively.

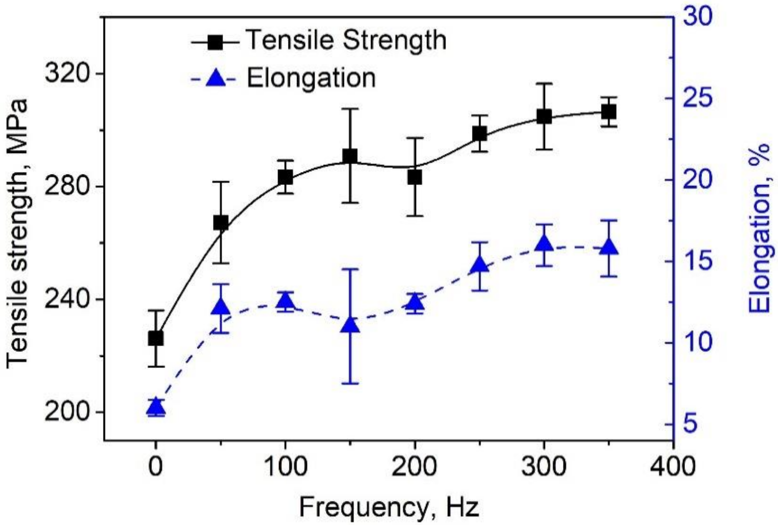

Figure 7. Effect of f on mechanical properties.

It can be concluded that the variation of mechanical properties of lock bottom welds were very consistent with the porosity, because the f threshold of pore elimination was

350 Hz at r as 0.6 mm, and the highest UTS and EL were achieved. That is, the pore defects were the main factor affecting the mechanical properties of laser welding of Al alloys in lock butt configuration. In addition, when f = 50 Hz, the porosity of the weld increased, but the mechanical properties improved, indicating that the pore defect was not the only factor affecting the mechanical properties. The strong stirring effect of the laser beam inhibited the growth of columnar grains and reduced the width of the coarse grain zone near the fusion line, which played an important role in the prevention of crack propagation during the tensile test of lock bottom welds. This will be discussed in detail in Section 3.5.

3.4. Fracture Modes and Morphologies

Figure 8 shows the cross section of the fracture of lock bottom welds. It was found that there were three fracture modes. Firstly, when 0 Hz $\leq f <$ 50 Hz, as shown in Figure 8a, there was a large pore with a diameter of 0.97 mm in the weld, and the weld was completely broken in the EQZ. Secondly, when 50 Hz $\leq f \leq$ 200 Hz, as shown in Figure 8b,c, there were small pores with a diameter of 0.39 mm in the weld. The inclination angle of the fracture line gradually decreased from nearly 90°, and the fracture position transferred from EQZ to CGZ. Finally, when $f >$ 200 Hz, as shown in Figure 8d, the pores were fully eliminated in the lock bottom weld. After the crack generated, it rapidly propagated to the EQZ, and then it passed directly through the CGZ to the HAZ under the maximum shear stress in the 45° direction, showing a typical pure shear fracture characteristic.

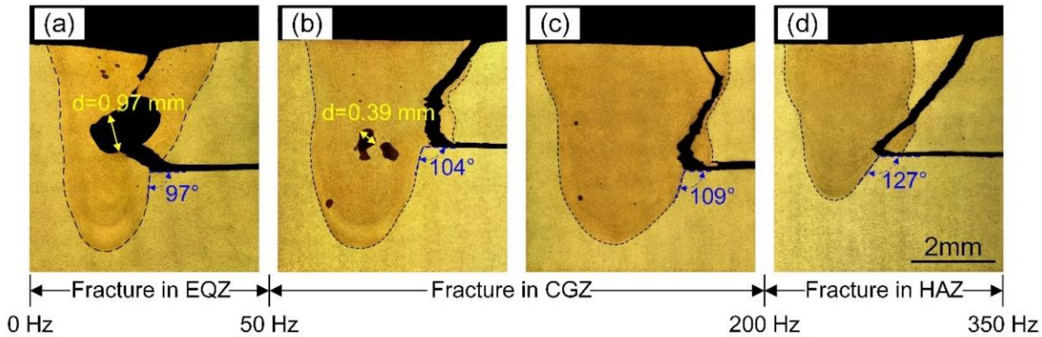

Figure 8. Fracture position of lock bottom welds, (**a**) f = 0 Hz, (**b**) f = 50 Hz, (**c**) f = 200 Hz, (**d**) f = 350 Hz.

As shown in Figure 9, all samples were characterized by ductile fracture with many dimples. In detail, as shown in Figure 9a,b, a large number of process pores appeared on the fracture surfaces of the weld without beam oscillation. However, as shown in Figure 9c–h, except for small pores at the fracture of weld fabricated with 50 Hz, other fractures had no obvious pores and their morphologies were flatter. According to fracture theories, the toughness was proportional to the dimple size. Similar results were obtained in this study, that is, the average dimple size of fracture at 350 Hz was 6.7 µm, which was larger than that of fracture without oscillation, showing a higher elongation.

3.5. Fracture Mechanism

According to the reported literature, the factors affecting the fracture are as follows: (1) Non-uniform stress distribution occurs at the defect section (such as pores), resulting in micro-cracks at the edge of the defect [30]; (2) Grain refinement can improve the ability of the weld to resist crack initiation and propagation [31]; (3) Welding structure and stress state. For example, in the T-joint, the initiation of cracks is mainly owed to the concentration of weld-induced residual stresses at the weld toe under shear stress [32].

Figure 10 shows the mechanism diagram of different fracture modes of lock bottom welds. It was found that, no matter what kind of fracture mode, the crack originated from the lock step. This was due to the special structure of the lock bottom weld. The BM thick side was prepared with process steps as the back support for the thin side of the BM; in the tensile process, the stress concentration occurred near the weld root of the BM thin side, which was shown in Figure 10a. It was the crack initiation position because the coarsened CGZ and overheated HAZ were the main microstructures near the weld fusion line. Notably, the weld actually bore the shear forces, because the stress center of the lock bottom weld was not on the same axis at the state of an uneven thickness. Moreover, the shear plane was located above the lock step, and the crack tended to expand upward after it was generated.

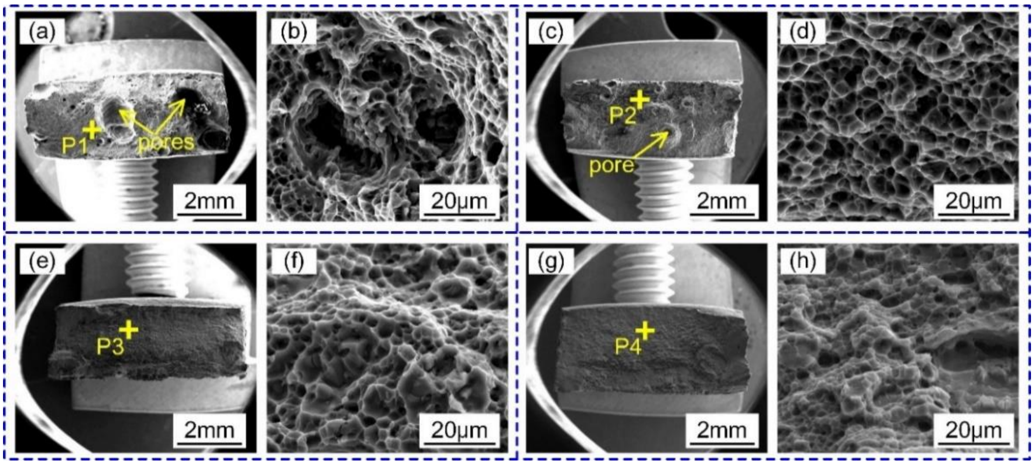

Figure 9. Morphologies of fracture surfaces, overviews of weld (**a**) #1, (**c**) #2, (**e**) #5 and (**g**) #8, details of (**b**) P1, (**d**) P2, (**f**) P3 and (**h**) P4.

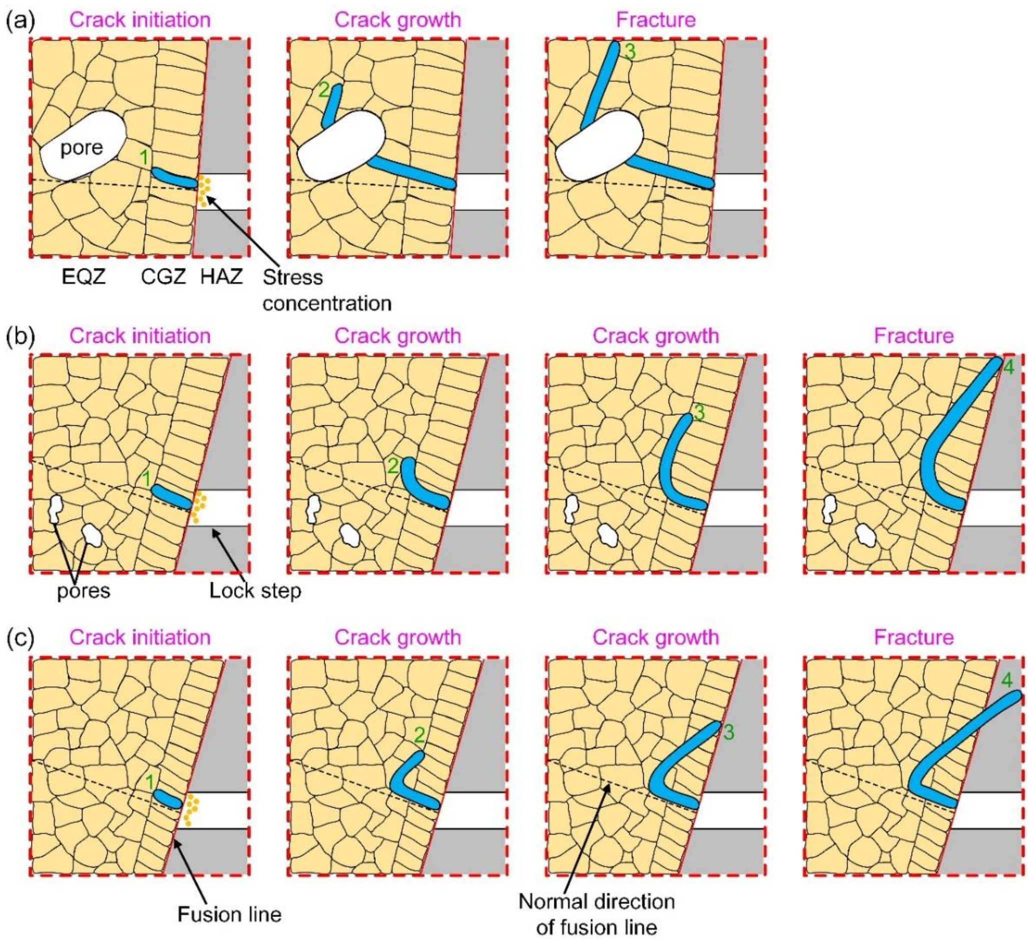

Figure 10. Fracture mechanism diagram, (**a**) fracture in EQZ, (**b**) fracture in CGZ, (**c**) fracture in HAZ.

As shown in Figure 10a, when 0 Hz $\leq f <$ 50 Hz, there were large pores in the weld, and the weak area around the pores was more likely to attract crack expansion. When the crack initiated from the lock step, it expanded in the direction of large pores. At the same time, the presence of large pores reduced the real load area during the tensile test, and the stress concentration was also prone to initiate cracks. Finally, the weld was completely broken in the EQZ.

As shown in Figure 10b, when 50 Hz $\leq f \leq$ 200 Hz, the angle between the fusion line and the lock step increased with f. Although there were pores in the weld, the size of the pores was small and located below the normal line of the fusion line, which meant that the pores were not in the direction of crack propagation. At this time, the influence of pores on crack propagation was reduced. After the crack initiation, it first propagated along the columnar grain boundary with the direction parallel to the normal direction of the fusion line. It kept the upward trend under the effect of shear stress as the crack went through the CGZ. However, the resistance of crack propagation increased because of the weld center forming fine equiaxed grains and possessing a high-volume fraction of grain boundaries [33]. Therefore, the crack propagated along the CGZ boundary for a certain distance and then re-entered the CGZ, and the weld finally fractured in the CGZ near the fusion line.

As shown in Figure 10c, when $f >$ 200 Hz, the pores in the lock bottom weld were eliminated and the width of the CGZ decreased to the minimum under the influence of beam oscillation. When the crack was generated, it propagated along the columnar grain boundary to EQZ, and then went directly through the CGZ to the HAZ in the direction of 45° under the maximum shear stress, showing a typical pure shear fracture characteristic. The weld finally fractured in the HAZ. Due to the short propagation distance of the crack in the CGZ, most cracks need to go through the EQZ and HAZ, which were more difficult for cracks to extend, because Schempp and Cross had demonstrated that the energy required for crack propagation in these two areas were greater than that of the CGZ [31]. UTS and EL were, then, greatly improved.

4. Conclusions

(1) Since the special structure form of the lock bottom weld and the crack originated from the lock step, the well-known fact in the field of oscillating laser welding that the stirring effect can generate more equiaxed grains and hence increase the strength of the weld, cannot fully explain the fracture behavior of the lock bottom weld. In order to reveal the fracture behavior of the lock bottom weld under the influence of the lock step, this paper studied the oscillating laser welded 5A06 aluminum alloy lock butt joint.

(2) Compared with lock bottom welds without beam oscillation, the temperature gradient of the molten pool decreased and growth of columnar grains was inhibited by beam oscillation, resulting in the reduction of width of the columnar grain zone (CGZ). The trend was strengthened with the increase of oscillation frequency (f), while the angle between the lock step and fusion line was increased.

(3) With the increase of f, the fracture angle between lock step and crack propagation line decreased from 90° to 45°. The fracture area during tensile tests transferred from equiaxed grain zone to CGZ and then to the heat affected zone when the width of the CGZ was narrow enough. The ultimate tensile strength and elongation of weld were increased up to 308 MPa and 18.2% respectively, showing an improvement of 36.3% and 203.3%.

Author Contributions: Y.L.: Conceptualization, Methodology, Writing–original draft. J.L.: Visualization, Investigation, Formal analysis. J.P.: Methodology, Software, Formal analysis, Data curation. X.L.: Visualization, Project administration. C.Z.: Writing-review & editing, Supervision. M.G.: Funding acquisition, Writing-review & editing, Supervision. All authors have read and agreed to the published version of the manuscript.

Funding: This research was financially supported by the National Natural Science Foundation of China (52205465, and 52205360) and the Aviation Science Foundation of China (20200054079001).

Institutional Review Board Statement: Not applicable.

Informed Consent Statement: Not applicable.

Data Availability Statement: The data presented in this study are available upon request from the corresponding author.

Conflicts of Interest: The authors declare no conflict of interest.

References

1. Yang, B.; Tan, C.; Zhao, Y.; Wu, L.; Chen, B.; Song, X.; Zhao, H.; Feng, J. Influence of ultrasonic peening on microstructure and surface performance of laser-arc hybrid welded 5A06 aluminum alloy joint. *J. Mater. Res. Technol.* **2020**, *9*, 9576–9587. [CrossRef]
2. Wu, D.; Li, W.; Liu, X.; Gao, Y.; Wen, Q.; Vairis, A. Effect of material configuration and welding parameter on weld formability and mechanical properties of bobbin tool friction stir welded Al-Cu and Al-Mg aluminum alloys. *Mater. Charact.* **2021**, *182*, 111518. [CrossRef]
3. Shin, Y.C.; Wu, B.; Lei, S.; Cheng, G.J.; Yao, Y.L. Overview of Laser Applications in Manufacturing and Materials Processing in Recent Years. *J. Manuf. Sci. Eng.* **2020**, *142*, 110818. [CrossRef]
4. Xie, J.; Chen, Y.; Yin, L.; Zhang, T.; Wang, S.; Wang, L. Microstructure and mechanical properties of ultrasonic spot welding TiNi/Ti6Al4V dissimilar materials using pure Al coating. *J. Manuf. Process.* **2021**, *64*, 473–480. [CrossRef]
5. Kenda, M.; Klobčar, D.; Bračun, D. Condition based maintenance of the two-beam laser welding in high volume manufacturing of piezoelectric pressure sensor. *J. Manuf. Syst.* **2021**, *59*, 117–126. [CrossRef]
6. Aminzadeh, A.; Parvizi, A.; Safdarian, R.; Rahmatabadi, D. Comparison between laser beam and gas tungsten arc tailored welded blanks via deep drawing. *Proc. Inst. Mech. Eng. Part B J. Eng. Manuf.* **2021**, *235*, 673–688. [CrossRef]
7. Zhu, B.; Zhang, G.; Zou, J.; Ha, N.; Wu, Q.; Xiao, R. Melt flow regularity and hump formation process during laser deep penetration welding. *Opt. Laser Technol.* **2021**, *139*, 106950. [CrossRef]
8. Hou, J.; Li, R.; Xu, C.; Li, T.; Shi, Z. A comparative study on microstructure and properties of pulsed laser welding and continuous laser welding of Al-25Si-4Cu-Mg high silicon aluminum alloy. *J. Manuf. Process.* **2021**, *68*, 657–667. [CrossRef]
9. Lin, R.; Wang, H.-P.; Lu, F.; Solomon, J.; Carlson, B.E. Numerical study of keyhole dynamics and keyhole-induced porosity formation in remote laser welding of Al alloys. *Int. J. Heat Mass Transf.* **2017**, *108*, 244–256. [CrossRef]
10. Tao, W.; Yang, S. Weld zone porosity elimination process in remote laser welding of AA5182-O aluminum alloy lap-joints. *J. Mater. Process. Technol.* **2020**, *286*, 116826. [CrossRef]
11. Feng, Y.; Gao, X.; Zhang, Y.; Peng, C.; Gui, X.; Sun, Y.; Xiao, X. Simulation and experiment for dynamics of laser welding keyhole and molten pool at different penetration status. *Int. J. Adv. Manuf. Technol.* **2021**, *112*, 2301–2312. [CrossRef]
12. Qi, N.; Zhan, X.; Chen, S.; Chen, D.; He, S. Effect of Laser Power on Tensile Performance of TA15 Laser-Welded Lock Bottom Joint. *Met. Mater. Int.* **2021**, *27*, 4645–4656. [CrossRef]
13. Zhang, R.; Tang, X.; Xu, L.; Lu, F.; Cui, H. Study of molten pool dynamics and porosity formation mechanism in full penetration fiber laser welding of Al-alloy. *Int. J. Heat Mass Transf.* **2020**, *148*, 119089. [CrossRef]
14. Tan, Z.; Pang, B.; Oliveira, J.; Chen, L.; Bu, X.; Wang, Z.; Cong, B.; Zeng, Z. Effect of S-curve laser power for power distribution control on laser oscillating welding of 5A06 aluminum alloy. *Opt. Laser Technol.* **2022**, *149*, 107909. [CrossRef]
15. Ahmadi, M.; Tabary, S.B.; Rahmatabadi, D.; Ebrahimi, M.; Abrinia, K.; Hashemi, R. Review of selective laser melting of magnesium alloys: Advantages, microstructure and mechanical characterizations, defects, challenges, and applications. *J. Mater. Res. Technol.* **2022**, *19*, 1537–1562. [CrossRef]
16. Liu, T.; Mu, Z.; Hu, R.; Pang, S. Sinusoidal oscillating laser welding of 7075 aluminum alloy: Hydrodynamics, porosity formation and optimization. *Int. J. Heat Mass Transf.* **2019**, *140*, 346–358. [CrossRef]
17. Chen, L.; Mi, G.; Zhang, X.; Wang, C. Effects of sinusoidal oscillating laser beam on weld formation, melt flow and grain structure during aluminum alloys lap welding. *J. Mater. Process. Technol.* **2021**, *298*, 117314. [CrossRef]
18. Fetzer, F.; Sommer, M.; Weber, R.; Weberpals, J.-P.; Graf, T. Reduction of pores by means of laser beam oscillation during remote welding of AlMgSi. *Opt. Lasers Eng.* **2018**, *108*, 68–77. [CrossRef]
19. Bi, J.; Liu, Z.; Chi, J.; Wang, H.; Tan, C.; Jia, X.; Yang, Z.; Starostenkov, M.D.; Dong, G. Formation mechanisms and control strategies of FQZ softening in Al–Li alloy welded joint. *J. Mater. Res. Technol.* **2023**, *23*, 2810–2823. [CrossRef]
20. Zhang, C.; Yu, Y.; Chen, C.; Zeng, X.; Gao, M. Suppressing porosity of a laser keyhole welded Al-6Mg alloy via beam oscillation. *J. Mater. Process. Technol.* **2020**, *278*, 116382. [CrossRef]
21. Hu, K.; Muneer, W.; Zhang, J.; Zhan, X. Effect of beam oscillating frequency on the microstructure and mechanical properties of dissimilar laser welding of AA2060 and AA6061 alloy. *Mater. Sci. Eng. A* **2022**, *832*, 142431. [CrossRef]
22. Wang, L.; Gao, M.; Zhang, C.; Zeng, X. Effect of beam oscillating pattern on weld characterization of laser welding of AA6061-T6 aluminum alloy. *Mater. Des.* **2016**, *108*, 707–717. [CrossRef]
23. Wang, Z.; Oliveira, J.; Zeng, Z.; Bu, X.; Peng, B.; Shao, X. Laser beam oscillating welding of 5A06 aluminum alloys: Microstructure, porosity and mechanical properties. *Opt. Laser Technol.* **2019**, *111*, 58–65. [CrossRef]
24. Li, S.; Mi, G.; Wang, C. A study on laser beam oscillating welding characteristics for the 5083 aluminum alloy: Morphology, microstructure and mechanical properties. *J. Manuf. Process.* **2020**, *53*, 12–20. [CrossRef]

25. Deng, H.; Chen, Y.; Jia, Y.; Pang, Y.; Zhang, T.; Wang, S.; Yin, L. Microstructure and mechanical properties of dissimilar NiTi/Ti6Al4V joints via back-heating assisted friction stir welding. *J. Manuf. Process.* **2021**, *64*, 379–391. [CrossRef]
26. Hagenlocher, C.; Sommer, M.; Fetzer, F.; Weber, R.; Graf, T. Optimization of the solidification conditions by means of beam oscillation during laser beam welding of aluminum. *Mater. Des.* **2018**, *160*, 1178–1185. [CrossRef]
27. Gong, J.; Li, L.; Meng, S.; Huang, R.; Zou, J.; Cao, H. Study on stability and microstructure properties of oscillating laser welded 5A06 alloy with narrow gap. *Opt. Laser Technol.* **2022**, *155*, 108360. [CrossRef]
28. Shi, L.; Li, X.; Jiang, L.; Gao, M. Numerical study of keyhole-induced porosity suppression mechanism in laser welding with beam oscillation. *Sci. Technol. Weld. Join.* **2021**, *26*, 349–355. [CrossRef]
29. Moshtaghi, M.; Safyari, M.; Mori, G. Combined thermal desorption spectroscopy, hydrogen visualization, HRTEM and EBSD investigation of a Ni–Fe–Cr alloy: The role of hydrogen trapping behavior in hydrogen-assisted fracture. *Mater. Sci. Eng. A* **2022**, *848*, 143428. [CrossRef]
30. Zhu, M.; Yang, S.; Bai, Y.; Fan, C. Microstructure and fatigue damage mechanism of 6082-T6 aluminium alloy welded joint. *Mater. Res. Express* **2021**, *8*, 056505. [CrossRef]
31. Schempp, P.; Cross, C.E.; Hacker, R.; Pittner, A.; Rethmeier, M. Influence of grain size on mechanical properties of aluminium GTA weld metal. *Weld. World* **2013**, *57*, 293–304. [CrossRef]
32. Zhao, Y.; Zhan, X.; Chen, S.; Bai, M.; Gong, X. Study on the shear performance and fracture mechanism of T-joints for 2219 aluminum alloy by dual laser-beam bilateral synchronous welding. *J. Alloys Compd.* **2020**, *847*, 156511. [CrossRef]
33. Mesbah, M.; Fadaeifard, F.; Nasiri-Tabrizi, B.; Matori, K.; Basirun, W. The impacts of grain boundary on the scattering of intermetallics in friction-stir-welded AA6061-T6. *Mater. Lett.* **2021**, *300*, 130206. [CrossRef]